

# Analytic Motion-compensated Region-of-Interest Reconstruction from Truncated Projections

Jan Hoskovec, Rolf Clackdoyle, Laurent Desbat and Simon Rit

**Abstract**—The aim of this work was to propose an analytic reconstruction of two-dimensional CT images in the presence of both patient motion and truncation of the projection data. The proposed method is based on the method of differentiated backprojection with Hilbert filtering (DBP-H). There is a variant of this algorithm which suits our purpose because it begins with a simple backprojection of the unprocessed projection data. The motion correction can be achieved by incorporating an analytic deformation compensation at the backprojections step, then the algorithm proceeds as usual. A simulation experiment was performed on a slice of the Shepp Logan phantom subject to a geometry-preserving deformation. The setup was such that the solutions of the deformation problem alone or of the truncation problem alone are known, but not that of both at the same time. The results demonstrate the efficacy of our approach, and that this type of reconstruction is feasible.

## I. INTRODUCTION

THIS work describes an analytic reconstruction method for two-dimensional (2D) motion-compensated tomographic image reconstruction from laterally truncated projection data. Combining region-of-interest (ROI) reconstruction with motion compensation is a challenging and pertinent issue in the field of tomography. So far, existing analytic methods only handle one problem or the other in isolation. ROI tomography has emerged during the 2000s [1] [2] [3] [4] [5] [6], after having been considered impossible for two decades. One of the main analytic reconstruction methods capable of handling lateral truncation belongs to the family of Differentiated Backprojection algorithms with Hilbert filtering (DBP-H), introduced in 2004 [1]. DBP-H algorithms can provide mathematically correct reconstructions along any line segment completely traversing the object provided this line segment remains completely visible in all projection views [5] [6]. Motion compensated reconstruction based on analytic motion models are known for a variety of motion classes, rigid, affine and even more general [7] [8] [9] [10]

This work was supported in part by a grant from la Région Rhône-Alpes and by grant no ANR-12-BS01-0018 (DROITE project) from the Agence Nationale de la Recherche (France).

Jan Hoskovec is with Laboratoire Hubert Curien ; CNRS UMR 5516 ; Université Jean Monnet, Saint-Étienne, France and with CREATIS ; CNRS UMR 5220 ; Inserm U1044 ; INSA-Lyon ; Université Claude Bernard - Lyon 1 ; Centre Léon Bérard, Lyon, France, e-mail: jan.hoskovec@univ-st-etienne.fr

Rolf Clackdoyle is with Laboratoire Hubert Curien ; CNRS UMR 5516 ; Université Jean Monnet, Saint-Étienne, France

Laurent Desbat is with TIMC-IMAG ; CNRS UMR 5525 ; Université Joseph Fourier - Grenoble 1, Grenoble, France

Simon Rit is with Université de Lyon, CREATIS ; CNRS UMR 5220 ; Inserm U1044 ; INSA-Lyon ; Université Claude Bernard - Lyon 1 ; Centre Léon Bérard, Lyon, France

[11]. However, although algorithms belonging to the DBP-H family are known to be capable of exact reconstruction from laterally truncated data [1] [5] and have been used in the context of motion-compensated reconstruction [9] [12], to our knowledge, handling both analytic motion compensation and truncated projections simultaneously is new.

## II. THEORY

### A. Notation

Let  $\vec{x} = (x, y)^T$  be a point in the image space, the origin being set at the center of rotation of the gantry. Let  $f(\vec{x})$  be the density function describing the imaged object. The parallel projections of this object are defined as (see Fig. 1 for illustration)

$$\bar{p}(s, \theta) = \int_{-\infty}^{\infty} f(s\vec{\theta} + r\vec{\theta}^\perp) dr \quad (1)$$

with

$$\vec{\theta} = \begin{pmatrix} -\sin \theta \\ \cos \theta \end{pmatrix} \quad (2)$$

$$\vec{\theta}^\perp = \begin{pmatrix} \cos \theta \\ \sin \theta \end{pmatrix} \quad (3)$$

and for fan-beam projections,

$$p(\alpha, \beta) = \int_0^{\infty} f(\vec{v}_\beta + t\vec{\alpha}) dt \quad (4)$$

with

$$\vec{v}_\beta = R \begin{pmatrix} \sin \beta \\ \cos \beta \end{pmatrix} \quad (5)$$

$$\vec{\alpha} = \begin{pmatrix} \sin(\alpha + \beta) \\ -\cos(\alpha + \beta) \end{pmatrix} \quad (6)$$

where the angles are measured counterclockwise and  $R$  is the radius of the source path.

It can be shown directly from (1) and (4) that

$$\bar{p}(s, \theta) = p(\alpha, \beta) \quad (7)$$

with

$$\theta = \alpha + \beta - \frac{\pi}{2} \quad (8)$$

$$s = R \sin \alpha \quad (9)$$

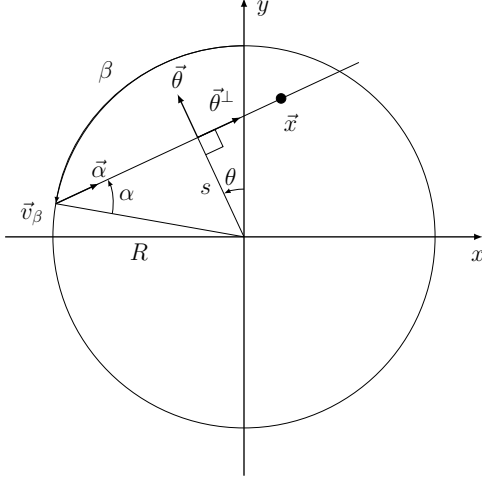


Figure 1. The fan-beam projection geometry. The source is at  $\vec{v}_\beta$  and the trajectory radius is  $R$ . A measurement ray in the fan-beam geometry is parametrized by  $(\alpha, \beta)$ . Also shown are the equivalent parameters  $(s, \theta)$  expressing the same ray in parallel projection geometry.

### B. Motion model

Following [11], we consider the restrictive class of motions that can be modelled by a geometry-preserving deformation  $\Gamma$ , which maps a fan to a different fan. The deformation is assumed to be known.

Mathematically, this deformation can be described by a bijective function  $\Gamma_\beta$  which depends on the gantry angle  $\beta$

$$\Gamma_\beta : [-\alpha_m, \alpha_m] \longrightarrow [-\alpha_m, \alpha_m] \quad (10)$$

with

$$\Gamma_\beta(-\alpha_m) = -\alpha_m \quad (11)$$

$$\Gamma_\beta(\alpha_m) = \alpha_m \quad (12)$$

for every value of  $\beta$ . The dynamic density function  $f_\beta(\vec{x})$ , which evolves with increasing gantry angle  $\beta$ , can be linked, via the deformation function  $\Gamma$ , to the reference object  $f_0$ :

$$f_\beta(\vec{x}) = f_\beta(\vec{v}_\beta + t\vec{\alpha}) = f_0(\vec{v}_\beta + t\vec{\alpha}') \quad (13)$$

for some  $t \in \mathbb{R}^+$ , where

$$\vec{\alpha}' = \begin{pmatrix} \sin(\Gamma_\beta(\alpha) + \beta) \\ -\cos(\Gamma_\beta(\alpha) + \beta) \end{pmatrix}. \quad (14)$$

### C. Method

Our reconstruction method is based on an algorithm from the DBP-H family. The principle of the DBP-H reconstruction lies in the following relation

$$b_\phi(\vec{x}) = -2\pi H_\phi f(\vec{x}) \quad (15)$$

where  $b_\phi(\vec{x})$  is defined as the backprojection of the differentiated parallel projections,

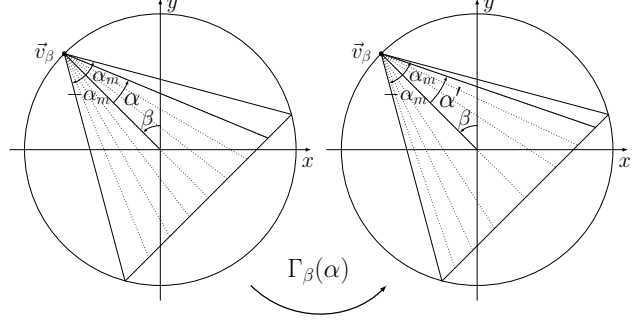


Figure 2. Geometry-preserving deformation: A fan in the reference image (left) will be transformed into a fan of the same size and position, but individual rays within the fan will be found under a different in-fan angle (right).

$$b_\phi(\vec{x}) = \int_{\phi}^{\phi+\pi} \frac{\partial}{\partial s} \bar{p}(s, \theta) \Big|_{s=\vec{x} \cdot \vec{\theta}} d\theta \quad (16)$$

and where  $H_\phi$  denotes Hilbert filtering along the vector  $\vec{\phi}^\perp = (\cos \phi, \sin \phi)^\top$  [1]. For  $\phi = 0$ , the Hilbert filtering will be carried out along the horizontal axis.

Equation (15) describes the backprojection from parallel projections with the partial derivative taking place along the detector, in sinogram space. Our aim being to reconstruct the image from a deformed fan-beam sinogram, the following changes will be made to the basic DBP-H method:

- 1) Switch the order of backprojection and derivative so that the latter takes place in the image space, thus allowing motion correction to take place immediately at backprojection time, without the complication of the derivative in the projections.
- 2) Convert the backprojection formula from parallel to fan-beam geometry.
- 3) Adapt the backprojection according to the deformation model.

Because we reverse the backprojection and differentiation steps, we prefer to use the name ‘‘BP-D-H’’ (for BackProjection-Derivative-Hilbert filtering), rather than the usual DBP(-H) for ‘‘Differentiated BackProjection’’ or the sometimes used BPF (BackProjection-Filtration).

1) *Backproject first*: Zeng [13] exchanges the order of the backprojection and the differentiation steps. The following result is obtained and can be demonstrated by evaluating the right hand side using the chain rule for differentiation.

$$b_\phi(\vec{x}) = \frac{\partial}{\partial x} b_{s,\phi}(\vec{x}) + \frac{\partial}{\partial y} b_{c,\phi}(\vec{x}) \quad (17)$$

where

$$b_{s,\phi}(\vec{x}) = \int_{\phi}^{\phi+\pi} \bar{p}(\vec{x} \cdot \vec{\theta}, \theta) (-\sin \theta) d\theta$$

$$b_{c,\phi}(\vec{x}) = \int_{\phi}^{\phi+\pi} \bar{p}(\vec{x} \cdot \vec{\theta}, \theta) (\cos \theta) d\theta$$
(18)

are backprojections from parallel projections, weighted by  $-\sin(\theta)$  and  $\cos(\theta)$  respectively.

2) *Fan-beam data*: We now need to modify (18) for full scan fan-beam data. First, if we use full scan parallel data, every ray is measured twice, once at  $\theta$  and a second time at  $\theta + \pi$ . To take this into account, we need to modify the  $\sin \theta$  and  $\cos \theta$  weighting terms so that they become  $\pi$ -periodic (in order for the weight to be the same for both measurements of the ray). The  $\pi$ -periodic weights are  $|\sin(\theta)|$  and  $\cos(\theta \bmod \pi)$  respectively.

Then we can do the change of variables to pass to fan-beam data. Using similar steps to Wei [14], we obtain the same formulas as in [13] and [14], up to the angular convention (see (8)) which modifies the weighting terms and makes a cosine expression appear in  $b_{s,\phi}$  and a sine expression in  $b_{c,\phi}$ :

$$b_{s,\phi}(\vec{x}) = -\frac{1}{2} \int_{\phi}^{\phi+2\pi} p(\alpha, \beta) |\cos(\alpha + \beta)| d\beta$$
(19)

$$b_{c,\phi}(\vec{x}) = -\frac{1}{2} \int_{\phi}^{\phi+2\pi} p(\alpha, \beta) (\sin(\alpha + \beta) \operatorname{sgn}(\cos(\alpha + \beta))) d\beta$$
(20)

where  $\alpha = \arcsin((x \cos \beta + y \sin \beta) / L)$  and where  $L$  is the ray length,  $L = \|\vec{x} - \vec{v}_{\beta}\|$ .

3) *Motion compensation*: When motion is present, the projections  $p_m$  of the dynamic image  $f_{\beta}$  can be linked to the static projections  $p$  by

$$p_m(\alpha, \beta) = \int_0^{\infty} f_{\beta}(\vec{v}_{\beta} + t\vec{\alpha}) dt = \int_0^{\infty} f_0(\vec{v}_{\beta} + t\vec{\alpha}') dt = p(\Gamma_{\beta}(\alpha), \beta)$$
(21)

Therefore, since  $\Gamma_{\beta}(\alpha)$  is bijective, we also have  $p(\alpha, \beta) = p_m(\Gamma_{\beta}^{-1}(\alpha), \beta)$ , and replacing the former by the latter in (19) and (20) yields the motion compensated backprojection formulas

$$b_{s,\phi} = -\frac{1}{2} \int_{\phi}^{\phi+2\pi} p_m(\Gamma_{\beta}^{-1}(\alpha), \beta) |\cos(\alpha + \beta)| d\beta$$
(22)

$$b_{c,\phi} = -\frac{1}{2} \int_{\phi}^{\phi+2\pi} p_m(\Gamma_{\beta}^{-1}(\alpha), \beta) (\sin(\alpha + \beta) \operatorname{sgn}(\cos(\alpha + \beta))) d\beta$$
(23)

with, again,  $\alpha = \arcsin((x \cos \beta + y \sin \beta) / L)$ .

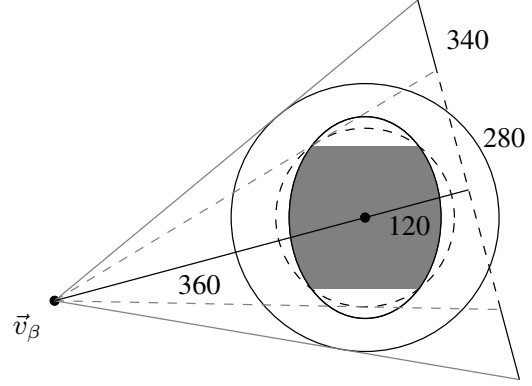


Figure 3. The elliptic phantom, the full (full circle) and reduced (dashed circle) fields-of-view and their associated detector lengths. Using a reduced field-of-view induces lateral truncation of the projections measured. In gray, the zone theoretically reconstructible from truncated projections using horizontal Hilbert filtering. See main text for an explanation of the dimensions of the detector and the two FOVs.

4) *Finite Hilbert inverse*: Combining (15) and (17) yields

$$\frac{\partial}{\partial x} b_{s,\phi}(\vec{x}) + \frac{\partial}{\partial y} b_{c,\phi}(\vec{x}) = -2\pi H_{\phi} f(\vec{x})$$
(24)

where  $b_{s,\phi}$  and  $b_{c,\phi}$  can be obtained either using (18) or (22) and (23), depending on whether we are using the static or motion-distorted sinogram. The last part of the reconstruction method consists of applying the inverse Hilbert transform to  $b_{\phi}$  (which equals the right hand side of (24)) to obtain the final image. As in [1], we used the finite Hilbert transform from [15] to invert  $H_{\phi} f(\vec{x})$ . In the following simulation, we used horizontal filtering,  $\phi = 0$ , and therefore this finite inversion was performed on horizontal lines. The a priori image support, on which this finite inversion is performed, was assumed to be completely contained within the disk centered at origin and with a radius of 120 mm (slightly larger than the major half-axis of the elliptic phantom).

5) *Truncation geometry*: Fig. 3 shows the full and limited FOV around our phantom. The smaller FOV intersects the phantom, causing truncation. The zone for which all horizontal lines are measured even with a reduced FOV, and therefore the DBP-H / BP-D-H reconstruction is theoretically possible [6], is highlighted in gray.

### III. SIMULATIONS

We tested our method on an off-center slice of the 3D Shepp-Logan phantom [16], whose support is an ellipse with half-axis lengths of 113 and 85 mm, for the following cases:

- 1) static phantom, no truncation
- 2) dynamic phantom, no truncation
- 3) static phantom, truncated and
- 4) dynamic phantom, truncated.

The deformation function used for the dynamic phantom was described in Desbat et al. [11]. Fig. 4 shows the phantom deformed by our function  $\Gamma_{\beta}(\alpha)$  for various values of  $\beta$ . The truncation was turned on and off by setting the detector length to different values. For the non truncated simulations,

the virtual flat detector had a length of 340 mm, yielding a field-of-view with a radius of approximately 150 mm. If the truncation was to be present, the virtual detector length was reduced to 280 mm, which in turn constrained the FOV radius to approximately 100 mm. In both cases, the source-to-detector distance was 480 mm and the source-to-isocenter distance was 360 mm. There were 768 projections generated for regularly sampled values of  $\beta$  between 0 and  $2\pi$ .

#### IV. DISCUSSION AND CONCLUSION

Fig. 5 shows the results of our simulation. The second column shows the catastrophic effect of uncorrected motion deformations. By comparing the bottom row to Fig. 3, we can note that the theoretical prediction of the reconstructible ROI was correct. Visually, there is little to no difference between the first and third column, therefore we can consider the motion compensation successful.

However, the horizontal profiles on Fig. 6 show a small underestimation of the reconstructed values in the motion compensated case, more visible in the truncated case. The exact source of this offset is currently under investigation and seems to be related to rounding errors and similar implementation problems.

As for future development, using multiple runs of the algorithm with different Hilbert filtering directions, we can expect to extend the correctly reconstructed ROI. It would also be interesting to adapt our algorithm to other motion models (for example, combining in-fan deformation as in here with source displacement). Multiple phantoms, truncation geometries and a test on noisy data or clinical data with artificially computed motion would also be interesting.

Overall, we consider this result to be a successful proof of concept and encouraging for our future work on CT reconstruction techniques aiming to handle truncation and motion compensation simultaneously.

#### REFERENCES

- [1] F. Noo, R. Clackdoyle, and J. D. Pack, "A two-step hilbert transform method for 2d image reconstruction," *Physics in Medicine and Biology*, vol. 49, no. 17, p. 3903, 2004.
- [2] R. Clackdoyle, F. Noo, J. Guo, and J. Roberts, "Quantitative reconstruction from truncated projections in classical tomography," *IEEE Trans Nucl Sci*, vol. 51, no. 5, pp. 2570–2578, Oct. 2004.
- [3] X. Pan, Y. Zou, and D. Xia, "Image reconstruction in peripheral and central regions-of-interest and data redundancy," *Medical physics*, vol. 32, no. 3, pp. 673–684, 2005.
- [4] Y. Zou, X. Pan, and E. Y. Sidky, "Image reconstruction in regions-of-interest from truncated projections in a reduced fan-beam scan," *Physics in medicine and biology*, vol. 50, no. 1, p. 13, 2005.
- [5] M. Defrise, F. Noo, R. Clackdoyle, and H. Kudo, "Truncated hilbert transform and image reconstruction from limited tomographic data," *Inverse Problems*, vol. 22, no. 3, p. 1037, 2006.
- [6] R. Clackdoyle and M. Defrise, "Tomographic reconstruction in the 21st century," *Signal Processing Magazine, IEEE*, vol. 27, no. 4, pp. 60–80, 2010.
- [7] C. Crawford, K. King, C. Ritchie, and J. Godwin, "Respiratory compensation in projection imaging using a magnification and displacement model," *IEEE Trans Med Imaging*, vol. 15, no. 3, pp. 327–332, 1996.

- [8] S. Roux, L. Desbat, A. Koenig, and P. Grangeat, "Exact reconstruction in 2d dynamic ct: compensation of time-dependent affine deformations," *Physics in medicine and biology*, vol. 49, no. 11, p. 2169, 2004.
- [9] H. Yu, Y. Wei, J. Hsieh, and G. Wang, "Data consistency based translational motion artifact reduction in fan-beam ct," *Medical Imaging, IEEE Transactions on*, vol. 25, no. 6, pp. 792–803, 2006.
- [10] H. Yu and G. Wang, "Data consistency based rigid motion artifact reduction in fan-beam ct," *Medical Imaging, IEEE Transactions on*, vol. 26, no. 2, pp. 249–260, 2007.
- [11] L. Desbat, S. Roux, P. Grangeat *et al.*, "Compensation of some time dependent deformations in tomography," *IEEE transactions on medical imaging*, vol. 26, no. 2, pp. 261–9, 2007.
- [12] L. Yu, Y. Zou, E. Y. Sidky, C. A. Pelizzari, P. Munro, and X. Pan, "Region of interest reconstruction from truncated data in circular cone-beam ct," *Medical Imaging, IEEE Transactions on*, vol. 25, no. 7, pp. 869–881, 2006.
- [13] G. L. Zeng, "Image reconstruction via the finite hilbert transform of the derivative of the backprojection," *Medical physics*, vol. 34, no. 7, pp. 2837–2843, 2007.
- [14] Y. Wei, "Comment on "image reconstruction via the finite hilbert transform of the derivative of the backprojection"[med. phys. 34, 2837–2843 (2007)]," *Medical physics*, vol. 34, no. 10, pp. 4068–4070, 2007.
- [15] S. G. Michlin and A. H. Armstrong, *Integral equations and their applications to certain problems in mechanics, mathematical physics and technology*. London, 1957.
- [16] A. C. Kak and M. Slaney, *Principles of Computerized Tomographic Imaging*. IEEE Press, 1988.



Figure 4. The deformed phantom visualized at different moments during the measurement. Due to different angular conventions here and in [11], the motion was parameterized by  $(\beta - \pi/2) \bmod 2\pi$  instead of just  $\beta$ . From left to right:  $\beta = 90^\circ$  (reference time),  $\beta = 210^\circ$ ,  $\beta = 10^\circ$ ,  $\beta = 89^\circ$ .

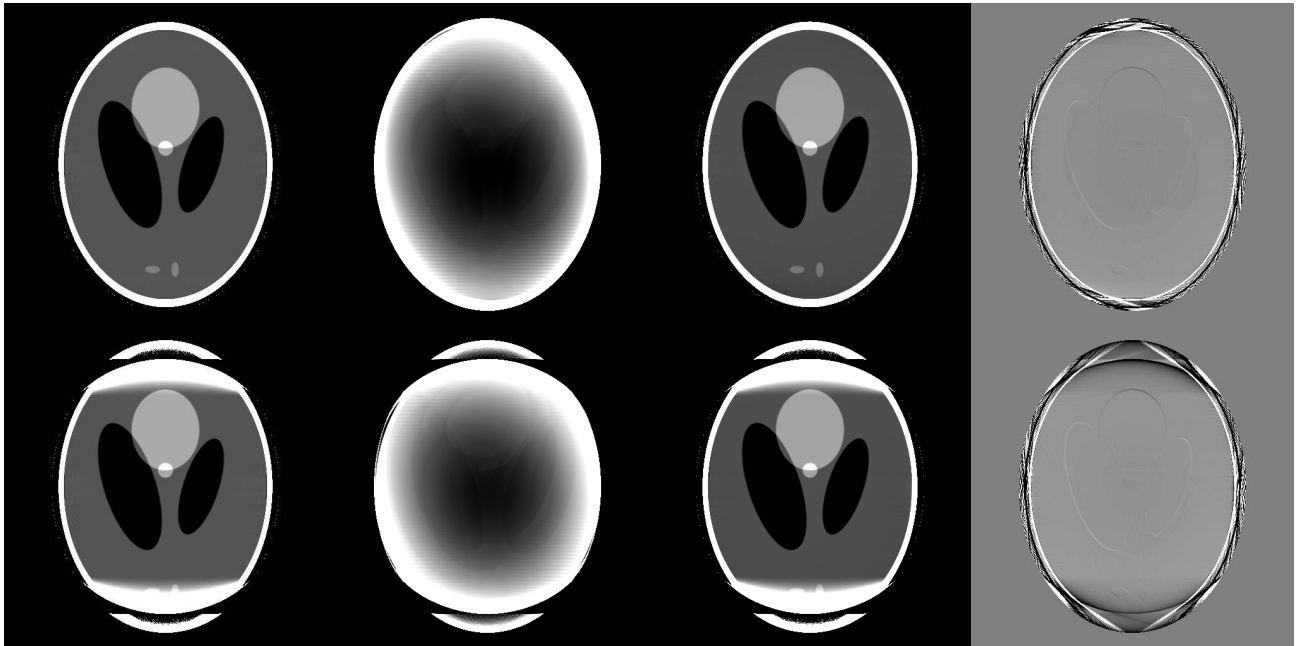


Figure 5. Top row: Reconstructions obtained from non-truncated data. Ratio of the phantom half-axes to FOV radius 4:3:5. Bottom row: Reconstructions from truncated data. Ratio of the phantom half-axes to FOV radius 12:9:10. Columns from left to right: 1. Reconstructions from static projections. Gray level range: [1.0,1.06]. 2. Reconstructions obtained from applying the static algorithm to dynamic projections. Gray level range: [0.8,1.2]. 3. Motion compensated reconstructions from dynamic projections. Gray level range: [1.0,1.06]. 4. Difference between static and motion-compensated reconstruction (column 1 - column 3). Gray level range: [-0.01,0.01].

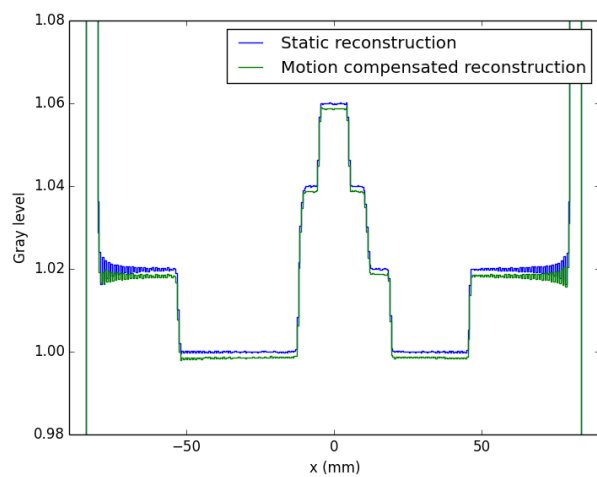
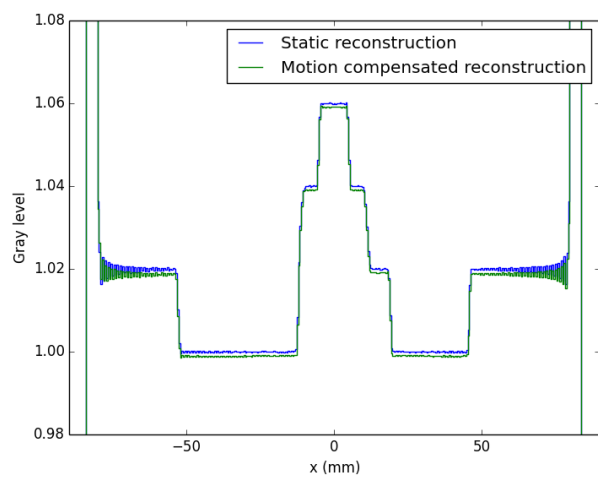


Figure 6. Horizontal profiles across the reconstructed image at  $y = 15.75$  mm. Left: Full data. Right: Laterally truncated data.